



High axial resolution imaging system for large volume tissues using combination of inclined selective plane illumination and mechanical sectioning

QI ZHANG,^{1,2} XIONG YANG,^{1,2} QINGLEI HU,^{1,2} KE BAI,^{1,2} FANGFANG YIN,^{1,2} NING LI,^{1,2} YADONG GANG,^{1,2} XIAOJUN WANG,^{1,2} AND SHAOQUN ZENG^{1,2,*}

¹Collaborative Innovation Center for Biomedical Engineering, Wuhan National Laboratory for Optoelectronics-Huazhong University of Science and Technology, Wuhan, Hubei 430074, China

²Britton Chance Center and MOE Key Laboratory for Biomedical Photonics, School of Engineering Sciences, Huazhong University of Science and Technology, Wuhan, Hubei 430074, China

*sqzeng@mail.hust.edu.cn

Abstract: To resolve fine structures of biological systems like neurons, it is required to realize microscopic imaging with sufficient spatial resolution in three dimensional systems. With regular optical imaging systems, high lateral resolution is accessible while high axial resolution is hard to achieve in a large volume. We introduce an imaging system for high 3D resolution fluorescence imaging of large volume tissues. Selective plane illumination was adopted to provide high axial resolution. A scientific CMOS working in sub-array mode kept the imaging area in the sample surface, which restrained the adverse effect of aberrations caused by inclined illumination. Plastic embedding and precise mechanical sectioning extended the axial range and eliminated distortion during the whole imaging process. The combination of these techniques enabled 3D high resolution imaging of large tissues. Fluorescent bead imaging showed resolutions of 0.59 μm , 0.47 μm , and 0.59 μm in the x, y, and z directions, respectively. Data acquired from the volume sample of brain tissue demonstrated the applicability of this imaging system. Imaging of different depths showed uniform performance where details could be recognized in either the near-soma area or terminal area, and fine structures of neurons could be seen in both the xy and xz sections.

© 2017 Optical Society of America

OCIS codes: (180.6900) Three-dimensional microscopy; (170.0180) Microscopy; (170.2520) Fluorescence microscopy; (170.3880) Medical and biological imaging.

References and links

1. A. Li, H. Gong, B. Zhang, Q. Wang, C. Yan, J. Wu, Q. Liu, S. Zeng, and Q. Luo, "Micro-Optical Sectioning Tomography to Obtain a High-Resolution Atlas of the Mouse Brain," *Science* **330**(6009), 1404–1408 (2010).
2. T. Ragan, L. R. Kadir, K. U. Venkataraju, K. Bahlmann, J. Sutin, J. Taranda, I. Arganda-Carreras, Y. Kim, H. S. Seung, and P. Osten, "Serial two-photon tomography for automated ex vivo mouse brain imaging," *Nat. Methods* **9**(3), 255–258 (2012).
3. H. Gong, S. Zeng, C. Yan, X. Lv, Z. Yang, T. Xu, Z. Feng, W. Ding, X. Qi, A. Li, J. Wu, and Q. Luo, "Continuously tracing brain-wide long-distance axonal projections in mice at a one-micron voxel resolution," *Neuroimage* **74**, 87–98 (2013).
4. H. Gong, D. Xu, J. Yuan, X. Li, C. Guo, J. Peng, Y. Li, L. A. Schwarz, A. Li, B. Hu, B. Xiong, Q. Sun, Y. Zhang, J. Liu, Q. Zhong, T. Xu, S. Zeng, and Q. Luo, "High-throughput dual-colour precision imaging for brain-wide connectome with cytoarchitectonic landmarks at the cellular level," *Nat. Commun.* **7**, 12142 (2016).
5. M. N. Economou, N. G. Clack, L. D. Levis, C. R. Gerfen, K. Svoboda, E. W. Myers, and J. Chandrasekar, "A platform for brain-wide imaging and reconstruction of individual neurons," *eLife* **2016**, 5 (2016).
6. H. U. Dodt, U. Leischner, A. Schierloh, N. Jährling, C. P. Mauch, K. Deininger, J. M. Deussing, M. Eder, W. Ziegler, and K. Becker, "Ultramicroscopy: three-dimensional visualization of neuronal networks in the whole mouse brain," *Nat. Methods* **4**(4), 331–336 (2007).
7. C. J. Niedworok, I. Schwarz, J. Ledderose, G. Giese, K. K. Conzelmann, and M. K. Schwarz, "Charting Monosynaptic Connectivity Maps by Two-Color Light-Sheet Fluorescence Microscopy," *Cell Reports* **2**(5), 1375–1386 (2012).

8. L. Silvestri, A. Bria, L. Sacconi, G. Iannello, and F. S. Pavone, "Confocal light sheet microscopy: micron-scale neuroanatomy of the entire mouse brain," *Opt. Express* **20**(18), 20582–20598 (2012).
9. E. A. Susaki, K. Tainaka, D. Perrin, F. Kishino, T. Tawara, T. M. Watanabe, C. Yokoyama, H. Onoe, M. Eguchi, S. Yamaguchi, T. Abe, H. Kiyonari, Y. Shimizu, A. Miyawaki, H. Yokota, and H. R. Ueda, "Whole-Brain Imaging with Single-Cell Resolution Using Chemical Cocktails and Computational Analysis," *Cell* **157**(3), 726–739 (2014).
10. R. Tomer, L. Ye, B. Hsueh, and K. Deisseroth, "Advanced CLARITY for rapid and high-resolution imaging of intact tissues," *Nat. Protoc.* **9**(7), 1682–1697 (2014).
11. M. Stefaniuk, E. J. Gualda, M. Pawlowska, D. Legutko, P. Matryba, P. Koza, W. Konopka, D. Owczarek, M. Wawrzyniak, P. Loza-Alvarez, and L. Kaczmarek, "Light-sheet microscopy imaging of a whole cleared rat brain with Thy1-GFP transgene," *Sci Rep-Uk* **6** (2016).
12. T. V. Truong, W. Supatto, D. S. Koos, J. M. Choi, and S. E. Fraser, "Deep and fast live imaging with two-photon scanned light-sheet microscopy," *Nat. Methods* **8**(9), 757–760 (2011).
13. R. K. Chhetri, F. Amat, Y. Wan, B. Höckendorf, W. C. Lemon, and P. J. Keller, "Whole-animal functional and developmental imaging with isotropic spatial resolution," *Nat. Methods* **12**(12), 1171–1178 (2015).
14. M. B. Bouchard, V. Voleti, C. S. Mendes, C. Lacefield, W. B. Grueber, R. S. Mann, R. M. Bruno, and E. M. C. Hillman, "Swept confocally-aligned planar excitation (SCAPE) microscopy for high speed volumetric imaging of behaving organisms," *Nat. Photonics* **9**(2), 113–119 (2015).
15. B. C. Chen, W. R. Legant, K. Wang, L. Shao, D. E. Milkie, M. W. Davidson, C. Janetopoulos, X. S. Wu, J. A. Hammer 3rd, Z. Liu, B. P. English, Y. Mimori-Kiyosue, D. P. Romero, A. T. Ritter, J. Lippincott-Schwartz, L. Fritz-Laylin, R. D. Mullins, D. M. Mitchell, J. N. Bembenek, A. C. Reymann, R. Böhme, S. W. Grill, J. T. Wang, G. Seydoux, U. S. Tulu, D. P. Kiehart, and E. Betzig, "Lattice light-sheet microscopy: Imaging molecules to embryos at high spatiotemporal resolution," *Science* **346**(6208), 1257998 (2014).
16. A. Kumar, Y. Wu, R. Christensen, P. Chandris, W. Gandler, E. McCreedy, A. Bokinsky, D. A. Colón-Ramos, Z. Bao, M. McAuliffe, G. Rondeau, and H. Shroff, "Dual-view plane illumination microscopy for rapid and spatially isotropic imaging," *Nat. Protoc.* **9**(11), 2555–2573 (2014).
17. K. M. Dean, P. Roudot, E. S. Welf, G. Danuser, and R. Fiolka, "Deconvolution-free Subcellular Imaging with Axially Swept Light Sheet Microscopy," *Biophys. J.* **108**(12), 2807–2815 (2015).
18. P. Hoyer, G. de Medeiros, B. Balázs, N. Norlin, C. Besir, J. Hanne, H. G. Kräusslich, J. Engelhardt, S. J. Sahl, S. W. Hell, and L. Hufnagel, "Breaking the diffraction limit of light-sheet fluorescence microscopy by RESOLFT," *Proc. Natl. Acad. Sci. U.S.A.* **113**(13), 3442–3446 (2016).
19. W. R. Legant, L. Shao, J. B. Grimm, T. A. Brown, D. E. Milkie, B. B. Avants, L. D. Lavis, and E. Betzig, "High-density three-dimensional localization microscopy across large volumes," *Nat. Methods* **13**(4), 359–365 (2016).
20. J. D. Manton and E. J. Rees, "triSPIM: light sheet microscopy with isotropic super-resolution," *Opt. Lett.* **41**(18), 4170–4173 (2016).
21. A. Kumar, R. Christensen, M. Guo, P. Chandris, W. Duncan, Y. Wu, A. Santella, M. Moyle, P. W. Winter, D. Colón-Ramos, Z. Bao, and H. Shroff, "Using Stage- and Slit-Scanning to Improve Contrast and Optical Sectioning in Dual-View Inverted Light Sheet Microscopy (diSPIM)," *Biol. Bull.* **231**(1), 26–39 (2016).
22. R. M. Power and J. Huysken, "A guide to light-sheet fluorescence microscopy for multiscale imaging," *Nat. Methods* **14**(4), 360–373 (2017).
23. Z. Yang, B. Hu, Y. Zhang, Q. Luo, and H. Gong, "Development of a Plastic Embedding Method for Large-Volume and Fluorescent-Protein-Expressing Tissues," *PLoS One* **8**(4), e60877 (2013).
24. H. Xiong, Z. Zhou, M. Zhu, X. Lv, A. Li, S. Li, L. Li, T. Yang, S. Wang, Z. Yang, T. Xu, Q. Luo, H. Gong, and S. Zeng, "Chemical reactivation of quenched fluorescent protein molecules enables resin-embedded fluorescence microimaging," *Nat. Commun.* **5**, 3992 (2014).
25. Y. D. Gang, H. F. Zhou, Y. Jia, L. Liu, X. L. Liu, G. Rao, L. H. Li, X. J. Wang, X. H. Lv, H. Q. Xiong, Z. Q. Yang, Q. M. Luo, H. Gong, and S. Q. Zeng, "Embedding and Chemical Reactivation of Green Fluorescent Protein in the Whole Mouse Brain for Optical Micro-Imaging," *Front Neurosci.* **11**, 121 (2017).
26. T. Zheng, Z. Yang, A. Li, X. Lv, Z. Zhou, X. Wang, X. Qi, S. Li, Q. Luo, H. Gong, and S. Zeng, "Visualization of brain circuits using two-photon fluorescence micro-optical sectioning tomography," *Opt. Express* **21**(8), 9839–9850 (2013).
27. D. Turaga and T. E. Holy, "Miniaturization and defocus correction for objective-coupled planar illumination microscopy," *Opt. Lett.* **33**(20), 2302–2304 (2008).
28. C. Bourgenot, C. D. Saunter, J. M. Taylor, J. M. Girkin, and G. D. Love, "3D adaptive optics in a light sheet microscope," *Opt. Express* **20**(12), 13252–13261 (2012).
29. D. Turaga and T. E. Holy, "Aberrations and their correction in light-sheet microscopy: a low-dimensional parametrization," *Biomed. Opt. Express* **4**(9), 1654–1661 (2013).
30. L. A. Royer, W. C. Lemon, R. K. Chhetri, Y. Wan, M. Coleman, E. W. Myers, and P. J. Keller, "Adaptive light-sheet microscopy for long-term, high-resolution imaging in living organisms," *Nat. Biotechnol.* **34**(12), 1267–1278 (2016).

Introduction

Any simple biological activities could be synergies of many fine structures in large scales, thus biomedical study has requirements to acquire imaging data with fine structures from large volume samples. In brain science research, combining mechanical sectioning with regular imaging methods, researchers could obtain high resolution images in large volume [1–5]. However, limited by optics principle, the axial resolution of these methods, which mostly above 1 micron, would not be equally high as lateral resolution. The mismatch of the lateral and axial resolutions has adverse effect on processing and analyzing of three dimensional fine structures.

Another kind of tool for fast sample imaging is microscopy based on light-sheet illumination. Using wide field imaging mode, combining with tissue optical clearing techniques, imaging results of large volume sample could be acquired within a short time [6–14]. Minimal phototoxicity and rapid acquisition make it a powerful tool for biological studies. Light-sheet microscopies have also shown capability to acquire high axial resolution ($<1\ \mu\text{m}$) in imaging of some thin samples ($<100\ \mu\text{m}$) [15–20]. Specifically, using ultrathin light sheet to illumination, lattice light-sheet microscopy could yield images of 370 nm axial resolution; with structure illumination mode (SIM), axial resolution could even be increased to 280nm [15]. However, this high resolution could only be achieved in a very thin sample such as one layer of cells. Some efforts have been made to increase the volume, e.g. a dual-view inverted selective plane illumination microscopy (diSPIM) could provide isotropic spatial resolution as well [16], whereas only small ($\sim 50\ \mu\text{m}$), transparent samples could be well suited. Recently, by using stage- and slit- scanning mode, larger FOV was achieved [21], but with the sample thickness still limited to small samples such as a few layers of cells or *C. elegans* embryos.

Actually, maintaining high resolution over large volume in light-sheet microscopies is a challenge [22]. Generally using low NA objective enlarges illumination area, but results in thick light-sheet, and lower spatial resolution perpendicular to the illumination direction. With many efforts, submicron level of axial resolution is hard to achieve. For instance, two-photon scanned light-sheet microscopy (2P-SPIM) achieved resolution of $1.3 \times 1.3 \times 2.0\ \mu\text{m}^3$ in several hundred micron scale [12]. In the similar scale, resolution of Isotropic Multi-View Light Sheet Microscopy is in the range of 1.1-1.7 μm [13]. Swept confocally-aligned planar excitation (SCAPE) microscopy use single objective to perform light-sheet illumination imaging, the theoretical lateral and axial resolutions are at 0.4-2 μm and 1-3 μm respectively over large FOV ($600 \times 1000 \times 550\ \mu\text{m}$) [14]. These large volume imaging methods are very useful for in vivo activity imaging due to high volume imaging speed. However, resolutions, especially axial resolutions, of these methods are partially sacrificed to obtain large FOVs, and not proper for fine morphological imaging of even larger volume.

To overcome this trade-off between high resolution and large volume, it is highly desired to adopt mechanical sectioning to extend imaging depth while high NA illumination objective could be used to provide high axial resolution and fast imaging speed.

Here, by combining mechanical sectioning strategy and inclined selective plane illumination, we report an imaging system here for acquiring isotropous resolution data set in large volume. Similar to diSPIM, we use a relatively high numerical aperture objective to generate a light sheet with a narrow waist and another orthogonal objective to collect fluorescence. The sample is embedded in resin for mechanical sectioning to reach an extended range in axial scale. With prior researches about plastic embedding techniques, fluorescence in tissues could be well maintained for high resolution imaging [23–25]. To restrain aberrations increased by plastic embedding, a thin layer of the sample surface will be imaged during one imaging process. Thus, we chose a sCMOS worked in sub-array mode to acquire images rapidly. The stage-scanning-only strategy was adopted to imaging the surface of whole sample. With precision surface sectioning, we acquired isotropic resolution data set in large volume.

Methods

The schematic diagram of the system is shown in Fig. 1(a). 488-nm laser beam (Cobolt 06-MLD 488nm, Cobolt) was expanded by two lenses, then compressed in one dimension by a cylindrical lens. The line illumination was then projected to surface of sample by a tube lens and illumination objective (40X water, NA 0.8, Nikon). Another same objective was used to collect fluorescence. A sCMOS (ORCA-Flash 4.0, Hamamatsu Photonic K. K.) was used as detector. The size of each pixel is $6.5 \times 6.5 \mu\text{m}$. A diamond knife was mounted in the system to remove imaged part of sample after each imaging process.

As two water immersion objectives were used, plastic embedded sample was fixed in a water tank which was mounted on a 3D precision motorized stage (X axis: ABL20020, Y axis: ANT130, Z axis: AVL125, Aerotech). The stage moves sample to imaging and sectioning in high position accuracy and repeatability. Along with rigidity due to plastic embedding, high-precision of imaging and sectioning were guaranteed.

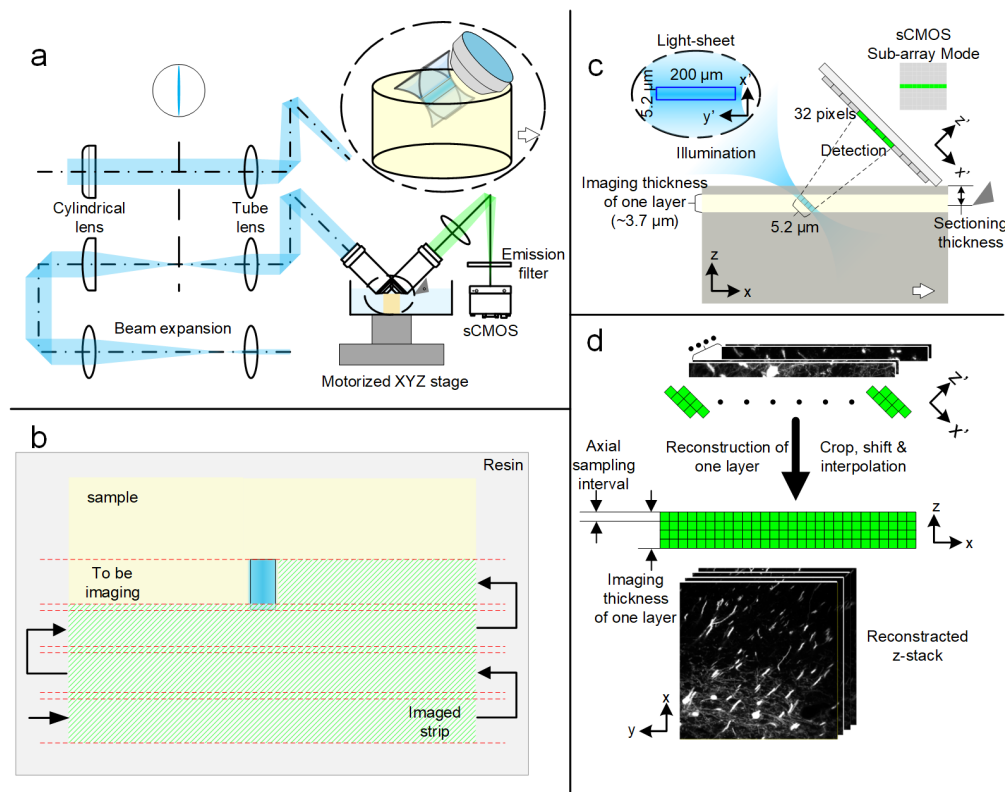


Fig. 1. (a) Optical scheme of selective plane illumination imaging system for extended large tissue. (b) Stage-scanning strategy of each layer for large tissue imaging. (c) Schematic representation of illumination with short Rayleigh range and detection with a sCMOS in sub-array mode. 32 lines activated pixels equals 5.2 μm in object space. The imaging thickness of one layer is $5.2 \mu\text{m} / \sin 45^\circ = 3.7 \mu\text{m}$. Sectioning thickness is slight less than imaging depth to ensure signal integrity. The activated pixels can be decreased to 16/8 lines for higher imaging quality, the effective light-sheet width and sectioning thickness should change accordingly. (d) Image reconstruction of oblique raw data.

The strategy of data acquiring is shown in Fig. 1(b), 1(c). We used a relatively high NA objective to form a thin light sheet. The available light-sheet width in y' direction was about 300 μm . While high NA brings short Rayleigh range, the thin light sheet would spread rapidly away from the focus. To exclude fluorescence from the away-from-focus area, we used a sCMOS in its sub-array mode as the detector. In this mode, only 8-32 lines of the detector

was activated. It was $1.3\text{--}5.2\mu\text{m}$ in x' direction at object space equivalently. The readout frequency in this mode could be much higher than that in full frame mode, which ensures the whole imaging time acceptability. The stage scanning strategy was applied to image large tissue. The stage moves the sample back and forth in x direction under objectives with an interval in y direction till the whole sample plane was imaged. In each strip, when the specimen is moved into field of interest, a signal generated by the stage controller will trigger sCMOS start to imaging in free-running mode (in free-running mode, sCMOS provides highest frame rate). The moving speed of stage is set to an appropriate value to match the sampling rate. The imaging length depends on frame number we set. The y direction interval is a little less than imaging strip width to avoid information loss.

As the focus plane of detection objective was neither parallel nor vertical to the surface of sample, to adapt to ordinary view, the images obtained by sCMOS required to be reorganized, shown in Fig. 1(d). During strip scanning, detector would capture a series of images which was oblique to surface of sample. We selected same lines of each frame, then stitched them together to form a new image which would be parallel to surface of sample. Applied a slight shift to each frame according to angle of inclination, and stacked those frames together, data set of one layer was informed. In short, in every imaging layer, we transform a series of original frames with 8-32 lines width in $x'\text{--}y'$ plane into 8-32 frames in $x\text{--}y$ plane. As the detection arm was inclined at 45° , sampling interval in z direction was $6.5\mu\text{m} \cdot \sin 45^\circ / 40 = 0.12\mu\text{m}$. Where $6.5\mu\text{m}$ is pixel size of sCMOS and 40 is magnification of objective. The newly formed data set have voxel size of $0.23 \times 0.16 \times 0.12\mu\text{m}$. After whole plane was imaged, surface of sample was sectioned with a diamond knife. To ensure no signal was lost, the section thickness was equal to or a slightly less than imaging thickness which was about $0.9\text{--}3.7\mu\text{m}$ [Fig. 1(c)]. Cycled imaging process and sectioning process, whole data set was acquired. With high programmable precision (100 nm) and feedback accuracy (20 nm) of the 3D precision motorized stage and rigidity of plastic embedding, the location error between two imaging processes was lot less than diffraction limit. Strip within same layer and frames from adjacent layer are registered naturally [4, 26].

Results and discussion

Measurement of lateral and axial point spread function

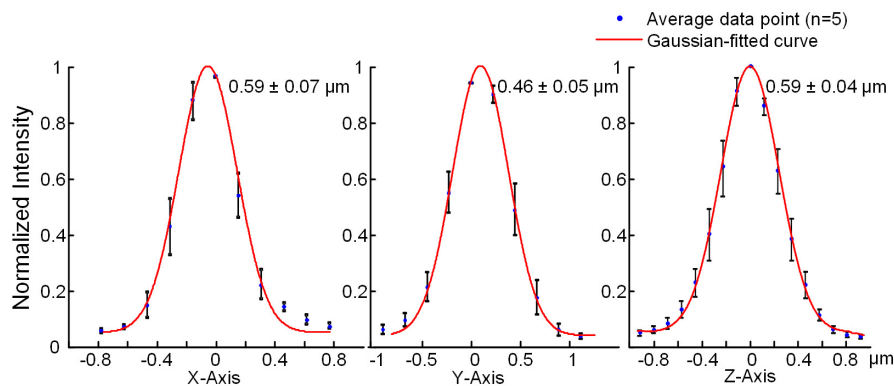


Fig. 2. Gaussian fit of 200 nm fluorescence beads signal intensity in x , y , and z direction. $N=5$.

200 nm fluorescent beads were used to measure spatial resolution of this system. $5\mu\text{m}$ thick resin film (refractive index, ~ 1.5) sectioning from a resin block was covered upon the beads to simulate actual imaging condition. Exposure time was set to 506 μs and the stage moved at a speed of 27.2 mm/min. 16 lines of sCMOS were activated. Stage step size in z -axis was set at $1.15\mu\text{m}$, thus 10 lines of origin images were used in each layer. Results were shown in Fig. 2. Full width of half maximum (FWHM) in x , y and z direction were $0.59 \pm 0.07\mu\text{m}$, $0.46 \pm$

0.05 μm , and $0.59 \pm 0.04 \mu\text{m}$ respectively. The resolution in x and z direction were slightly worse than that in y direction because point spread function (PSF) in x and z direction contained component of z' direction which was suffered more aberrations.

Aberrations caused by mismatch of refractive index

The average refractive index of tissue embedded in resin is above 1.45, while the immersion fluid refractive index is 1.33. This severely index mismatch will arise aberrations. In traditional forms of microscopy, the sample-saline interface is approximately perpendicular to the optical axis. In this situation, the aberration will be mostly spherical aberration which is relatively readily to be corrected. Tilted illumination makes total aberration more severe, as new aberrations will be introduced. Using some optical optimization and wavefront modulation methods, these complicated aberrations could be corrected to some extent [27–30]. However, those methods were mostly based on simplified models, it was difficult to make an ideal illumination beam in a heterogeneous sample. Even in a simplified model, the correction could only be well optimized for a specific narrow region of illumination light [29]. That means even with adaptive optics (AO), keeping the profile of illumination beam in a relatively long distance will still be difficult, which leads to contradiction of extended FOV and high illumination quality. As shown in Fig. 3, with the illumination depth increased, the illumination beam waist got thicker [Fig. 3(b)], which decreased axial resolution [Fig. 3(c)]. Meanwhile, the emission signal would be effected for the same reason. Simulation results showed that the deterioration of PSF were more significant in x' direction [Fig. 3(b)]. Our imaging strategy restricted imaging depth in superficial layer (under 10 μm) of sample and kept imaging area narrow to reduce effect of sample scattering and aberration caused by refractive index mismatch.

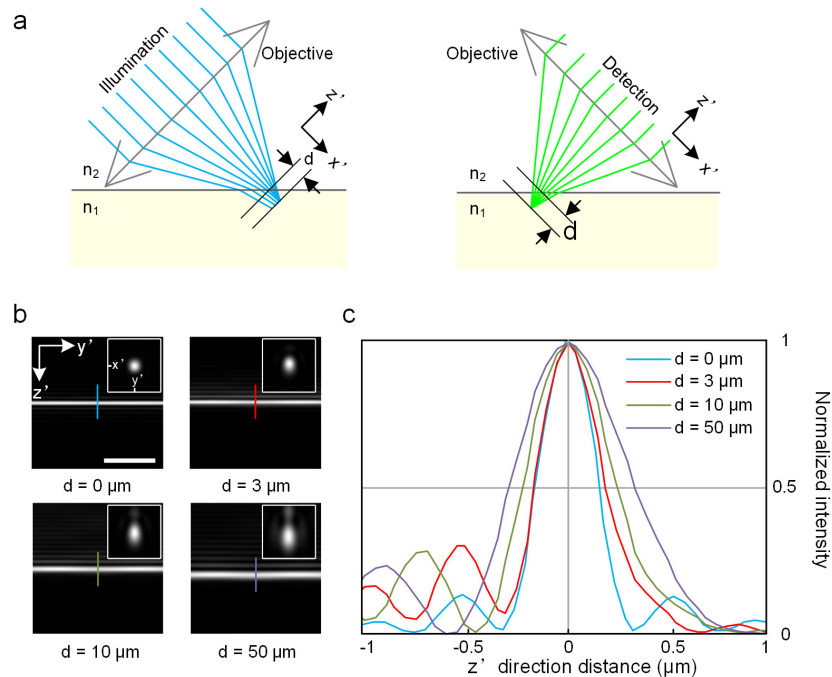


Fig. 3. (a) Aberration caused by mismatch of refraction index. (b) Zemax simulation results of illumination beam waists and detection PSFs (inserts) in different invasion depths, $n_1 = 1.45$, $n_2 = 1.33$. Size of inserts, $1.6 \times 1.6 \mu\text{m}$. (c) Intensity curves along z' direction lines in each result of (b). Scale bar, 5 μm .

High axial resolution imaging

To demonstrate high axial resolution of this system, we took confocal microscopy (Zeiss LSM710) as a reference. Figure 4(a), 4(b) showed maximum intensity projection of 20 μm z-stack acquired by each methods. As our imaging system required mechanical sectioning, an embedded Thy1-EGFP mouse brain tissue was used [Fig. 4(a)]. 16 lines of sCMOS was activated to detect signal. The voxel size was $0.23 \times 0.16 \times 0.12 \mu\text{m}^3$. To unified the voxel size in three-dimension, the result was then downsampling to $0.23 \times 0.23 \times 0.23 \mu\text{m}^3$. Meanwhile, for confocal imaging system, a 50 μm thick thy1-GFP mouse brain slice was chose as sample because it might be more suitable for confocal imaging than embedded ones. Results of first 20 μm thick near the surface was exhibited because tissue scattering which will decrease confocal imaging quality was not notable in this range. The voxel size was $0.23 \times 0.23 \times 0.23 \mu\text{m}^3$ while the exposure time of each pixel was set to 3.1 μs . Theoretically, the resolution of confocal microscopy is determined by objective. The lateral and axial resolution are commonly calculated with two equations: $r_{\text{lateral}} = 0.4 \lambda / \text{NA}$ and $r_{\text{axial}} = 1.4 \lambda \eta / \text{NA}^2$, where λ is emitted light wavelength, NA is the numerical aperture of the objective and η is the index of refraction. Using a high NA objective (Plan-Apochromat 40X/1.4 Oil DIC), confocal microscopy should have lateral resolution of 0.15 μm , and axial resolution of 0.56 μm . As shown in Fig. 4, the fine structures could be observed in both xy section and xz section from the inclined selective plane illumination imaging result [Fig. 4(a)]. As for the confocal microscopy, the xy section has a better quality than former one due to a high NA objective. In xz section, some blur effects appeared. Results demonstrated high axial resolution of this system.

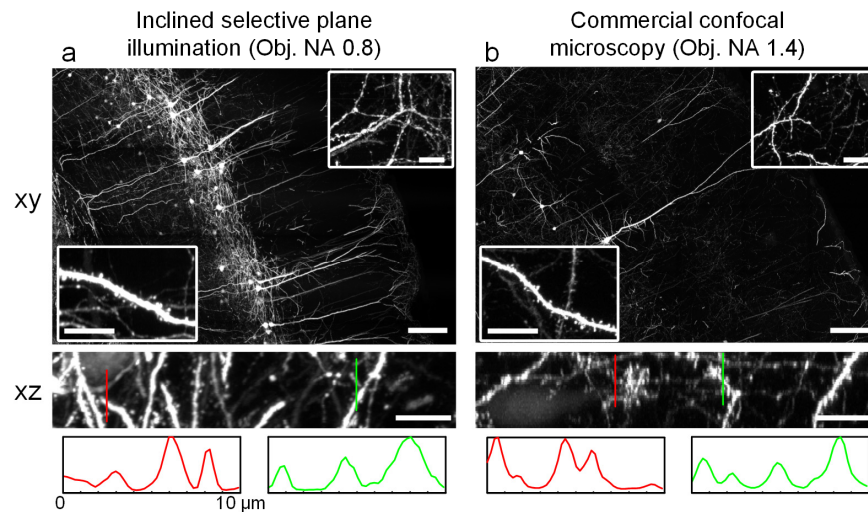


Fig. 4. Inclined selective plane illumination imaging and confocal imaging results using Thy1 GFP mouse. (a) xy section and xz section of selective plane illumination imaging result (12 imaging layers with 1.8 μm intervals). Inserts show enlarged views of neural fiber near soma and dendrite terminal area respectively. Normalized intense curves of the lines in xz sections shows at the bottom. (b) Similar to (a), except for the result is acquired by confocal microscopy (90 imaging planes with 0.23 μm axial intervals). Scale bar; xy sections, 100 μm , inserts and xz sections, 10 μm .

Volume imaging result

A Thy1-EGFP-labeled transgenic mouse brain was used to demonstrate this imaging system. The brain was excised and embedded in HM20 resin. Part of this brain tissue was imaged. The imaged part was 1800 $\mu\text{m} \times 1000 \mu\text{m} \times 1000 \mu\text{m}$ in x, y and z direction respectively [Fig. 5(a)].

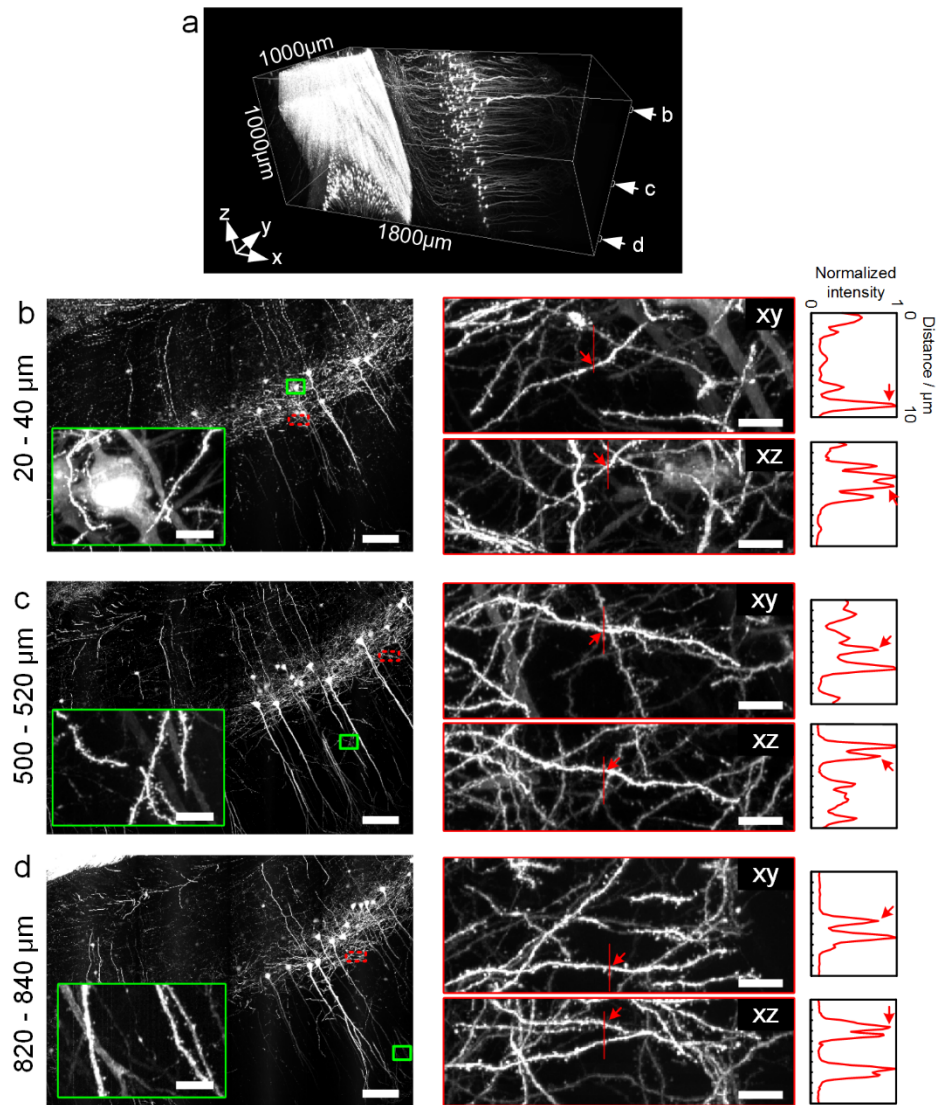


Fig. 5. Volume imaging result of mice brain tissue. (a) $1800 \times 1000 \times 1000 \mu\text{m}^3$ volume result of a Thy-1 GFP mice brain. (b) (c) (d) Images from different depth of the brain tissue. Note that the depth labels are only used to mark location as the surface imaging strategy is adopted. Left ones are 20 μm z-stack projections cropped from different depth imaging planes. The depth represents the distance from the original surface of this sample. The inserts show zoom-in views of green solid line boxes. Images on the right are xy sections and xz sections of the red dash line boxes. Curve diagrams profile the intensity along the lines in relevant images. Arrows point to the same fiber in each depth respectively. Scale bars: left ones, 100 μm , inserts and right ones, 10 μm .

We used 32 lines sub-array mode to capture images. During one strip imaging, the stage moved in x direction at speed of 47.8 mm/min, while the exposure time was set to 204 μs . The reconstructed images would have the pixel size of $0.23 \times 0.16 \mu\text{m}$ in x and y direction respectively. The axial interval was 2.76 μm , which was equivalent to thickness of 24 frames. Thus, 8 frames overlap area would exist between two layers to avoid information lost and to calibrate images if necessary. To image the entire volume, 362 imaging layers needed to be applied, and each layer contained 5 strips. With 204 μs exposure time, one strip imaging cost 1.25 s. the total exposure time was about $2.25 \text{ s} \times 5 \times 362 = 1.14 \text{ h}$. However, tissue

sectioning and non-exposure stage moving cost some extra time. The total imaging time was about 1.6 hours. Figure 5 shows the imaging result. Imaging of different depths showed uniform performance [Fig. 5(b)-5(d)]. Details could be recognized at either near-soma area or terminal area. With high resolution in all three dimensions, neuronal fibers can be distinguished even in those area with dense signals. In both xy and xz sections, fibers appeared the same width and fine structures of neurons can be seen.

Imaging speed

Generally speaking, imaging systems using light-sheet illumination usually have high imaging speed. Whole mouse brain data could be obtained in hours. However, for those applications, high sampling density is not necessary. Thus using low magnification objectives and applying coarse axial interval, high imaging speed could be realized. To reveal fine neural structures in 3D, high sampling density in either lateral or axial direction is required. Under this situation, we have to sacrifice imaging speed. Currently, this system was performed well, considering that the sampling speed of this system was close to the frame rate limitation of sCMOS which none imaging system could surpass. Using this imaging system, whole mouse brain ($\sim 500 \text{ mm}^3$) imaging needs about two weeks. Meanwhile, to store this 16 bit data set, about 200 TB storage space is required, which could be a challenge.

Conclusion

Here we describe an imaging system with inclined selective plane illumination for isotropic 3D imaging in large tissue. Combining selective plane illumination methods and mechanical sectioning of plastic embedded sample, this imaging system achieves high 3D resolution in extended large volume. Recently several imaging systems which can acquire high resolution data set in large tissues have been developed. Such as serial two-photon tomography (STP), fluorescence micro-optical sectioning tomography (fMOST), and two-photon fluorescence micro-optical sectioning tomography (2p-fMOST). With mechanical sectioning, these systems are able to achieve high lateral resolution with high imaging speed, but axial resolution is defective. Meanwhile light-sheet based imaging system acquired high axial resolution in relatively thin sample. The conflict between FOV and light-sheet thickness becomes a limitation. Here combined advantages of mechanical sectioning strategy and selective plane illumination, high 3D resolution in large volume can be achieved. High NA objective provides thin light-sheet illumination. Imaging in sample surface eliminates most tissue scattering and optical aberration, even none of optical clearing technique was applied. Plastic embedding ensures registration between layers and keeps interface between sample and immersion fluid smooth which will restrain artifacts caused by illumination. High read-out speed of sCMOS in sub-array mode provides a high imaging speed. It is a feasible system for large tissue imaging when high axial resolution is necessary. Meanwhile, some improvements could be implemented. Adaptive optics could be used to shape illumination beam. The strategy that one-time mechanical sectioning after several layers of imaging could be applied. Thus, the image quality and imaging speed remain a promotion.

Funding

Program 973 (2015CB755603); NSFC (2012YQ030260 and 81327802).

Acknowledgments

We thank X. Liu, X. Lv, L. Liu and other members of Britton Chance Center for Biomedical Photonics for advices.

Disclosures

The authors declare that there are no conflicts of interest related to this article.